catalysts

MDPI

Article

Boosting Photocatalysis: Cu-MOF Functionalized with g-C_3N_4 QDs for High-Efficiency Degradation of Congo Red

Yuhao Wang [1,2], Yuan Yang [3], Xinyue Zhang [1], Yajie Shi [1], Qiang Liu [1,*] and Keliang Wu [1]

[1] Henan Key Laboratory of Microbialfermentation, School of Biology and Chemical Engineering, Nanyang Institute of Technology, Nanyang 473000, China
[2] State Key Laboratory Incubation Base for Green Processing of Chemical Engineering, School of Chemistry and Chemical Engineering, Shihezi University, Shihezi 832003, China
[3] Petrochemical Engineering College, Bayingolin Vocational and Technical College, Korla 841000, China
* Correspondence: 3131077@nyist.edu.cn

Abstract

In recent years, organic dye contamination has posed a significant threat to water safety. This study presents a novel composite photocatalyst comprising graphitic carbon nitride quantum dots (g-C3N4QDs) supported on a copper-based metal–organic framework (Cu-MOF) for efficient visible-light degradation of organic pollutants. The g-C_3N_4QDs were synthesized via a facile strategy and subsequently immobilized onto the Cu-MOF support. Comprehensive characterization including SEM, TEM, XRD, BET, UV-Vis DRS, PL, and EIS confirmed the successful formation of a heterostructure, revealing that an optimized loading of g-C_3N_4QDs significantly enhanced light absorption, facilitated charge separation, and increased the specific surface area, with the optimal composite exhibiting 273 m^2/g compared to 112 m^2/g for the pristine Cu-MOF. Electrochemical analyses indicated a 2.38-fold enhancement in photocurrent density and a reduced interfacial charge transfer resistance, reflecting superior electron–hole pair separation. Crucially, the optimized g-C_3N_4QDs/Cu-MOF composite demonstrated exceptional photocatalytic performance, achieving 96.6% degradation of Congo red (100 mg/L) within 30 min under visible light irradiation, substantially outperforming the 77.6% degradation attained by the pristine Cu-MOF. This enhancement is attributed to the synergistic effects of improved light harvesting, efficient interfacial charge transfer across the heterojunction, and an enlarged active surface area. The composite exhibits considerable potential as a high-performance and stable photocatalyst for purifying dye-contaminated wastewater.

Keywords: metal–organic frameworks (MOFs); Cu-based MOF; C_3N_4QDs; heterojunction; light degradation performance

check for updates

Academic Editors: Keith Hohn and Leonarda Liotta

Received: 22 October 2025
Revised: 3 December 2025
Accepted: 9 December 2025
Published: 16 December 2025

Citation: Wang, Y.; Yang, Y.; Zhang, X.; Shi, Y.; Liu, Q.; Wu, K. Boosting Photocatalysis: Cu-MOF Functionalized with g-C_3N_4 QDs for High-Efficiency Degradation of Congo Red. *Catalysts* **2025**, *15*, 1169. https://doi.org/10.3390/catal15121169

Copyright: © 2025 by the authors. Licensee MDPI, Basel, Switzerland. This article is an open access article distributed under the terms and conditions of the Creative Commons Attribution (CC BY) license (https://creativecommons.org/licenses/by/4.0/).

1. Introduction

The development of industrialization has led to the extensive release of organic pollutants into the environment, posing serious threats to human health and ecosystems. These pollutants exhibit bioaccumulative characteristics and can propagate through the food chain, causing various health issues [1–3]. Moreover, their persistence under natural conditions results in prolonged environmental presence, disrupting ecological balance across diverse ecosystems [4,5]. Conventional chemical and physical methods for organic pollutant treatment often suffer from high costs, low efficiency, and a tendency to generate secondary contaminants [6–8]. In contrast, photocatalytic degradation offers high efficiency and favorable environmental compatibility. This method relies on photocatalysts

that generate holes and electrons under illumination, thereby initiating redox reactions with organic pollutants and decomposing them into harmless small molecules [9–11]. The selection of appropriate photocatalysts and optimization of reaction conditions represent critical factors in achieving high performance [12–14].

In recent years, photocatalytic research has increasingly focused on enhancing the activity, stability, and selectivity of photocatalysts, as well as exploring more efficient reaction systems and conditions [15–17]. Metal–organic frameworks (MOFs), a class of porous network materials composed of metal ions as nodes and organic ligands as bridging components [18,19], have been widely applied in pollutant removal through adsorption, catalysis, and membrane separation [20,21]. The high tunability and compositional diversity of MOFs enable the derivation of MOF-based materials with excellent stability and diverse active sites [22], while the loading of semiconductor materials or construction of active interfaces can further enhance light absorption and charge separation efficiency [23]. Porphyrins, as important photosensitive organic compounds, have been extensively utilized in constructing MOF photocatalysts. Porphyrin-based MOFs, synthesized from metal clusters and porphyrin ligands, exhibit attractive photosensitive properties and good stability, with the N_4 sites in porphyrin providing an ideal platform for anchoring catalytic metal centers [24]. Moreover, the rich microporous and mesoporous structures of porphyrin MOFs not only facilitate rapid pollutant adsorption but also isolate contaminants from complex environments, enabling effective pollutant enrichment [25]. These advantages make porphyrin MOF-based visible-light systems highly suitable for degrading organic pollutants in water.

Despite these merits, practical applications of MOFs face challenges such as material stability and the efficiency of photogenerated electron separation and transfer [26,27], underscoring the importance of MOF modification. Copper-based porphyrin MOFs (Cu-Porphyrin MOFs) have attracted significant attention in photocatalysis due to their unique photoelectronic properties and structural tunability. The MOF structure formed by Cu^{2+} and porphyrin ligands (e.g., TCPP) exhibits strong visible-light absorption—arising from porphyrin π–π^* transitions and metal–ligand charge transfer—and demonstrates efficient photogenerated carrier separation [28]. Additionally, Cu-MOFs typically possess high specific surface areas, ordered pore structures, and abundant active sites, which promote reactant adsorption and photocatalytic processes [29]. The construction of Z-scheme heterojunctions (e.g., Cu/In-PMOFs/$CdIn_2S_4$) has achieved efficient interfacial charge transport, yielding a photocatalytic hydrogen evolution rate far exceeding that of individual components [28], thereby providing a reference for designing high-performance MOF-based heterojunction photocatalysts. Notably, Cu-MOF exhibits good stability and reusability under visible-light irradiation, offering distinct advantages in organic pollutant degradation [30]. Research from the University of Strasbourg has shown that precise control over the metallization ratio of porphyrin ligands can optimize the photocatalytic performance of Cu-Porphyrin MOFs, such as enhancing CH_4 selectivity in CO_2 reduction reactions. Therefore, utilizing Cu-MOF as a support for constructing heterojunction photocatalysts represents an effective strategy for improving photocatalytic performance [31].

g-C_3N_4QDs not only inherit the high stability and environmental friendliness of graphitic carbon nitride (g-C_3N_4) [32] but also emerge as promising alternative materials due to their distinctive electrical and optical properties [33–35]. As demonstrated by Shi et al. [36], 5 nm $BiVO_4$QDs exhibit superior photocatalytic activity compared to conventional bulk quantum dots, which is attributed to their broader bandgap (2.66 eV) and enhanced quantum size effects that stimulate stronger photoelectric responses [37]. With a bandgap energy of 2.7 eV, g-C_3N_4QDs absorb visible light up to 450 nm, enabling efficient photocatalytic performance under visible light irradiation and demonstrating

strong adsorption capacity. Furthermore, g-C_3N_4 QDs effectively activate molecular oxygen to generate superoxide radicals for photocatalytic processes. Their unique triazine or tri-s-triazine ring structures confer excellent thermal stability and acid-base resistance, supporting diverse applications in CO_2 reduction and pollutant degradation. In the study by Wang et al. [38], CQDs/NH_2-MIL-125 composites were synthesized, showing that carbon quantum dot modification not only facilitates the separation of photogenerated charges but also enhances light energy conversion efficiency from visible to near-infrared regions.

This study aims to construct a g-C_3N_4QDs/Cu-MOF heterojunction composite photocatalyst for synergistic performance enhancement. The design rationale builds upon the quantum size effect of g-C_3N_4QDs modulating their energy band structure to broaden the photoresponse range and facilitate photogenerated electron–hole pair separation, combined with the high specific surface area and ordered porous architecture of Cu-MOF providing abundant pathways for reactant adsorption and diffusion. This configuration not only enhances visible-light harvesting but also drives directional migration of photogenerated charge carriers, effectively suppressing their recombination and thereby offering a novel pathway for improved photocatalytic degradation efficiency. Through systematic modulation of g-C_3N_4QD loading levels, this work investigates their regulatory effects on the composite's microstructure, photoelectrical properties, and photocatalytic performance, aiming to provide experimental and theoretical foundations for designing high-performance MOF-based photocatalytic materials.

2. Result and Discussion

2.1. Characterization

Figure 1 displays the XRD patterns of Cu-MOF and its composites with varying loadings of g-C_3N_4QDs (1 mL, 5 mL, and 10 mL). All samples exhibit characteristic diffraction peaks corresponding to the crystalline structure of Cu-MOF. The observed peaks, particularly at 2θ values of approximately 7.7°, 12.9°, and 18.8°, can be indexed to the (110), (210), and (400) crystal planes of the copper-porphyrin MOF (Cu-TCPP) structure, respectively, which aligns well with previous reports on similar materials. No shift in peak positions is observed after g-C_3N_4QDs incorporation, indicating that the host framework remains intact [39,40]. An increase in diffraction intensity with higher QD loading suggests enhanced crystallinity and improved structural ordering. The sharp and well-defined peaks reflect a highly ordered lattice and uniform crystallite size, corroborating the high crystallinity achieved in the synthesis. No additional peaks are detected, confirming the phase purity of the composite photocatalysts. These XRD results, combined with complementary morphological analyses, verify the successful formation of the g-C_3N_4QDs/Cu-MOF heterostructure.

The morphological features of the as-synthesized Cu-MOF and its composites with varying g-C_3N_4QD loadings (1, 5, and 10 mL) were investigated by scanning electron microscopy (SEM). As shown in Figure 2a, pure Cu-MOF exhibits a microspherical architecture composed of interconnected nanosheets, forming flower-like aggregates with diameters of approximately 10 μm. Figure 2b–d reveal that the hierarchical morphology remains intact after g-C_3N_4QDs incorporation, indicating that the loading process does not alter the fundamental framework structure. Energy-dispersive X-ray spectroscopy (EDS) mapping in Figure 2e demonstrates a homogeneous distribution of C, N, O, and Cu elements throughout the composite, confirming successful and uniform doping. TEM imaging (Figure 2f) further corroborates the nanosheet-assembled microstructure, consistent with SEM observations. High-resolution TEM (Figure 2g) reveals distinct lattice fringes with an interplanar spacing of 0.26 nm, corresponding to the crystalline planes of g-C_3N_4QDs, which provides direct evidence for the successful formation of the g-C_3N_4QDs/Cu-

MOF heterostructure. Table 1 presents the element content data obtained through the Mapping scan.

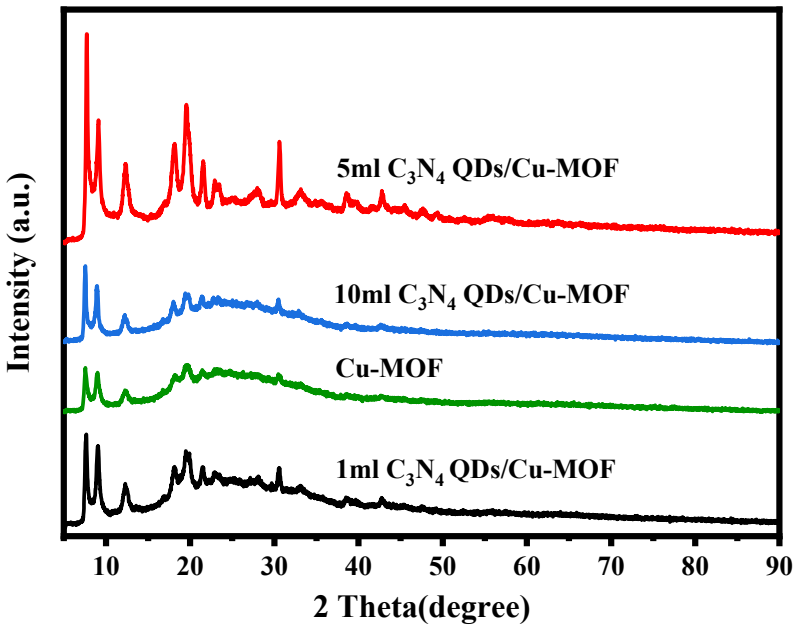


Figure 1. XRD patterns of the sample catalysts.

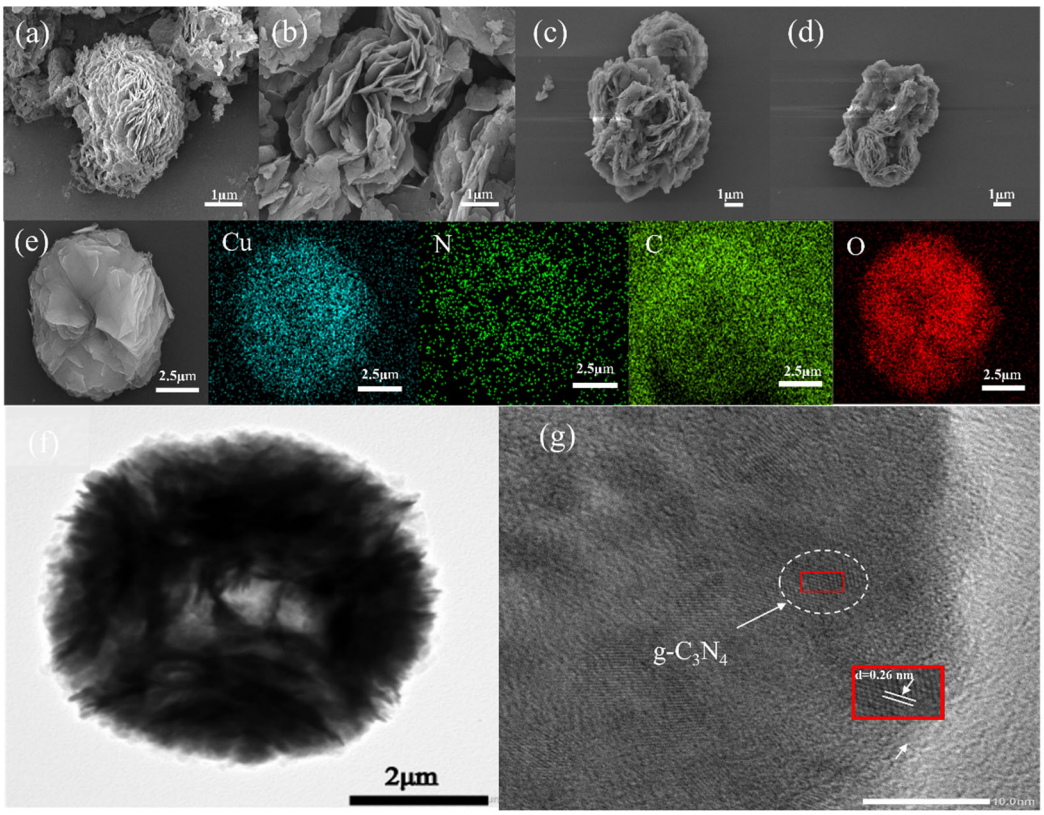


Figure 2. SEM diagram of the sample catalyst (**a**) Cu-MOF, (**b**) 1 mL g-C_3N_4QDs/Cu-MOF, (**c**) 5 mL g-C_3N_4QDs/Cu-MOF, (**d**) 10 mL g-C_3N_4QDs/Cu-MOF, (**e**) EDS elemental mapping images of 5 mL g-C_3N_4QDs/Cu-MOF The, (**f**) TEM plot of the 5 mL g-C_3N_4QDs/Cu-MOF, (**g**) HRTEM.

Table 1. Element content distribution.

Element	wt%	σ
Cu	9.8	0.5
N	5.0	0.5
O	43.1	0.5
C	42.1	0.5

The chemical composition and bonding states of Cu-MOF were analyzed by X-ray photoelectron spectroscopy (XPS) without any surface etching. The binding energy scale was calibrated by referencing the adventitious carbon C 1s peak to 284.8 eV to compensate for surface charging effects. The survey spectrum in Figure 3a confirms the presence of C, O, N, and Cu as the primary elements. High-resolution C 1s spectrum (Figure 3b) exhibits three characteristic peaks at binding energies of 284.8 eV, 286.5 eV, and 288.8 eV, corresponding to C–C, C–O–C, and O–C=O bonds [41], respectively. The O 1s spectrum (Figure 3c) displays peaks at 531.8 eV, 533.0 eV, and 534.2 eV, assigned to Cu–O, C=O, and C–O species. In the N 1s region (Figure 3d), contributions from C=N, C–N, and Cu–N bonds are observed at 397.9 eV, 399.8 eV, and 401.9 eV, respectively. The Cu 2p spectrum (Figure 3e) shows spin–orbit doublets at 934.1 eV (Cu $2p_{3/2}$) and 954.9 eV (Cu $2p_{1/2}$), along with satellite peaks at 939.9 eV, 943.8 eV, and 963.5 eV, characteristic of Cu^{2+} oxidation state. It is noted that these bonding features are also present in g-C_3N_4QDs, and the overlap of carbon species signals makes it challenging to distinguish g-C_3N_4QDs solely based on XPS data [42].

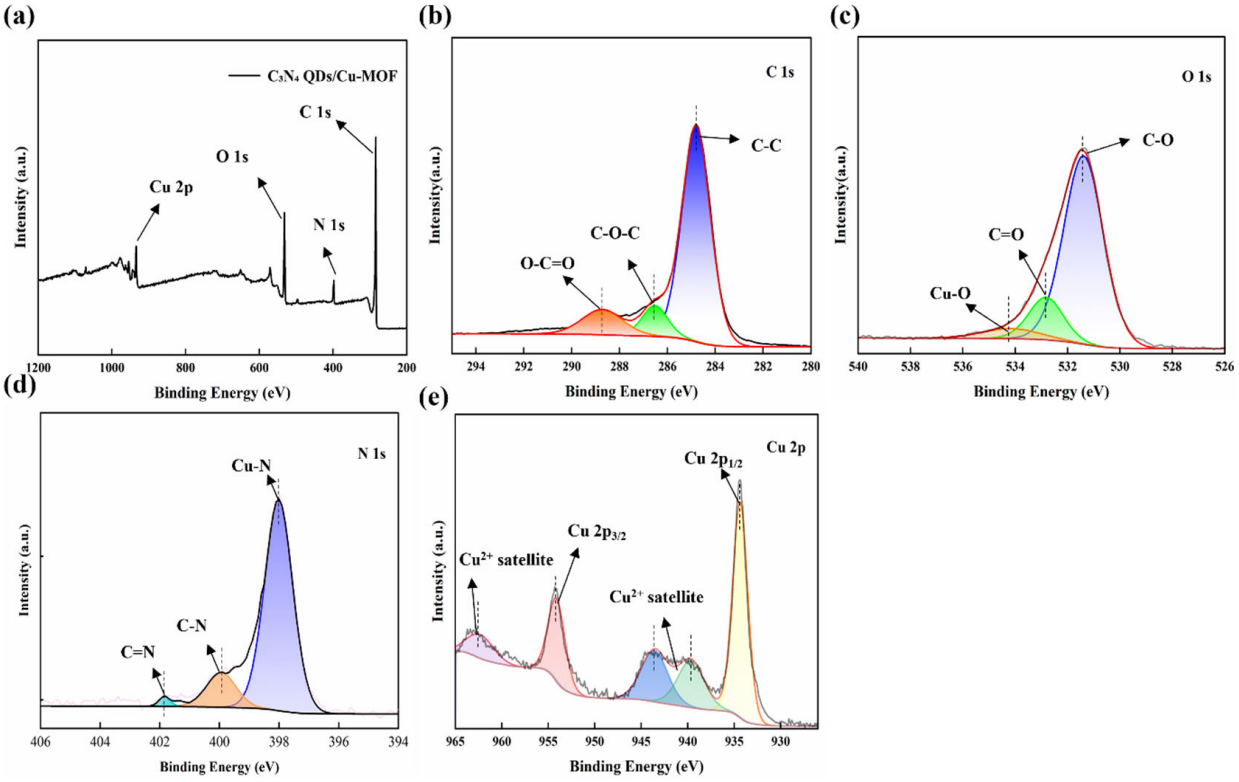


Figure 3. XPS spectrum of the sample catalyst (**a**) survey spectra, (**b**) C 1s, (**c**) O 1s, (**d**) N 1s, (**e**) Cu 2p.

The light absorption properties of Cu-MOF and its composites with different g-C_3N_4QD loadings (1, 5, and 10 mL) were investigated by UV-Vis diffuse reflectance spectroscopy. As shown in the absorption spectra (Figure 4a,c), all samples exhibit similar absorption edges in the visible region. The corresponding Tauc plots (Figure 4b,d)

reveal a redshift in the absorption edge for the 5 mL g-C_3N_4QDs/Cu-MOF composite, indicating an extension of light harvesting into the visible range. The optical bandgaps, determined from the intercept of the tangent to the absorption edge using the equation Eg = 1240/λg [43], are estimated to be 2.91 eV for Cu-MOF and 2.6 eV for C_3N_4. Notably, the 5 mL g-C_3N_4QDs/Cu-MOF composite demonstrates a distinct redshift, expanded visible-light absorption range, reduced transition energy, and enhanced absorption capability, representing the optimal performance among the prepared samples.

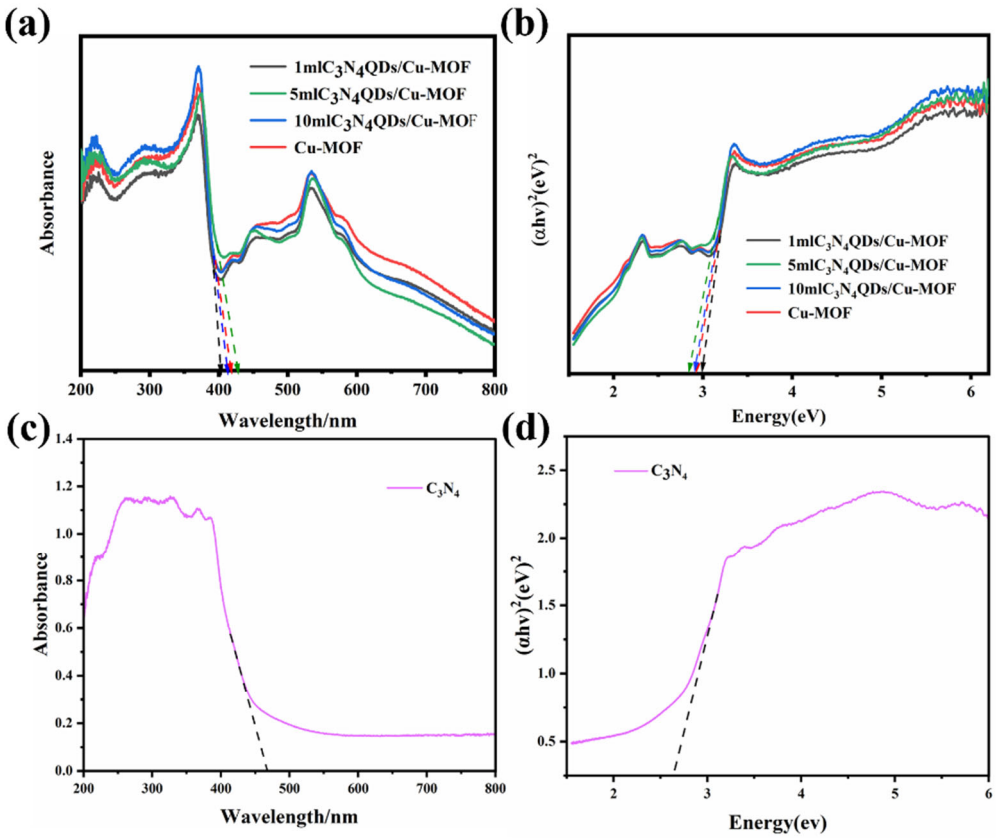


Figure 4. (**a**) UV-Vis diffuse reflectance spectra (DRS) of Cu-MOF and its composites with varying loadings of g-C_3N_4 QDs, (**b**) corresponding Tauc plots of the composites. (**c**) UV-Vis absorption spectrum of pure g-C_3N_4 QDs. (**d**) Tauc plot for g-C_3N_4 QDs. (Dotted lines in (**a**,**c**) denote the absorption edges used for bandgap calculation. Dashed lines in (**b**,**d**) represent the linear fits in Tauc plots for Eg determination).

Figure 5 presents the nitrogen adsorption–desorption isotherms and pore size distribution curves of the synthesized catalysts. The measured specific surface areas, summarized in the accompanying Table 2, indicate that the incorporation of g-C_3N_4QDs effectively inhibits the recombination of photogenerated electron–hole pairs. The BET analysis reveals a progressive increase in specific surface area with higher QD loading, with the 5 mL g-C_3N_4QDs/Cu-MOF composite exhibiting the largest surface area, reduced pore size, and enhanced porosity. These structural characteristics contribute to shortened electron transport paths and facilitated charge carrier separation. However, excessive QD loading leads to pore blockage, thereby diminishing photocatalytic efficiency.

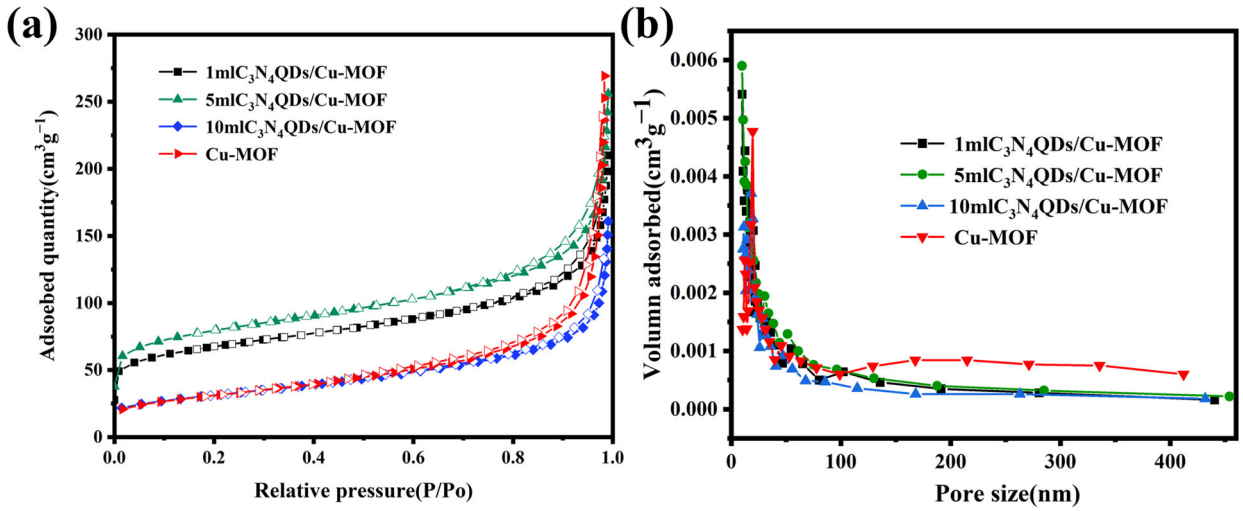


Figure 5. (**a**) Nitrogen adsorption–desorption isotherms of 1 mL C_3N_4QDs/Cu-MOF, 5 mL C_3N_4QDs/Cu-MOF, 10 mL C_3N_4QDs/Cu-MOF, and Cu-MOF, (**b**) pore size distribution curves of 1 mL C_3N_4QDs/Cu-MOF, 5 mL C_3N_4QDs/Cu-MOF, 10 mL C_3N_4QDs/Cu-MOF, and Cu-MOF.

Table 2. The BET data.

Sample	Specific Surface Area (m^2/g)	Pore Volume (cm^3/g)	Average Aperture (nm)
Cu-MOF	112.257	0.4487	74.6
1 mL C_3N_4QDs/Cu-MOF	230.059	0.3265	28.4
5 mL C_3N_4QDs/Cu-MOF	273.335	0.3981	29.1
10 mL C_3N_4QDs/Cu-MOF	111.225	0.3265	44.8

2.2. Photoluminescence Spectra and Photoelectric Properties

Steady-state photoluminescence (PL) emission spectroscopy was employed to investigate the separation and transfer behavior of photogenerated electron–hole pairs, highlighting the beneficial role of quantum dots and the MOF framework [44]. The steady-state photoluminescence spectrum was measured under an excitation light of λ_{ex} = 301 nm. The PL intensity, which reflects the efficiency of charge carrier recombination, decreases in the order: Cu-MOF > 1 mL g-C_3N_4QDs/Cu-MOF > 10 mL g-C_3N_4QDs/Cu-MOF > 5 mL g-C_3N_4QDs/Cu-MOF (Figure 6a). The composite with 5 mL g-C_3N_4QDs exhibits the lowest emission intensity, indicating the most efficient charge transfer and the highest suppression of electron–hole recombination among the samples [45]. To gain a deeper understanding of the optical properties of g-C_3N_4 QDs, we tested its excitation spectrum graph (Figure 6b).

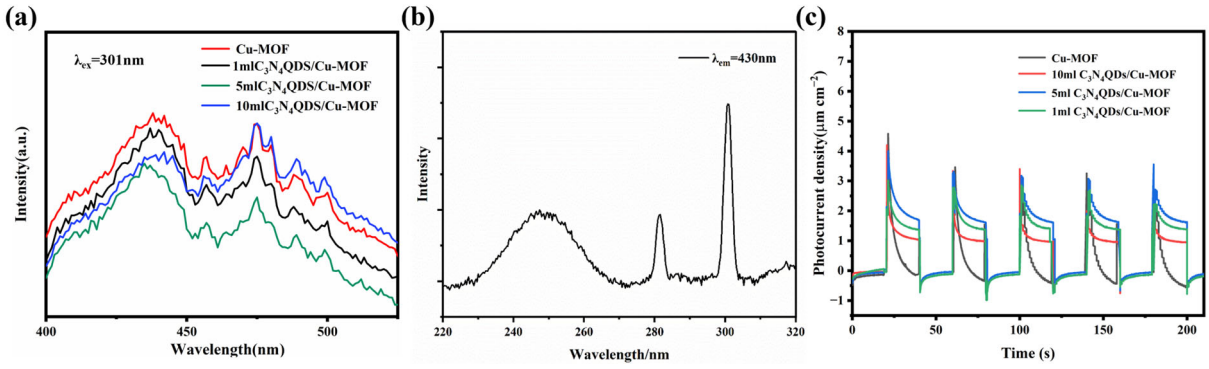


Figure 6. (**a**) Photoluminescence spectrum of the sample catalyst, (**b**) the excitation spectrum of the optimal sample and (**c**) the photocurrent response curve of the sample catalyst.

Electrochemical measurements were conducted to further elucidate the charge separation and transfer behavior. As shown in Figure 6c, the photocurrent density increases in the order: Cu-MOF < 10 mL g-C_3N_4QDs/Cu-MOF < 1 mL g-C_3N_4QDs/Cu-MOF < 5 mL g-C_3N_4QDs/Cu-MOF. Correspondingly, the Nyquist arc radii decrease sequentially [46] (Figure 7a), with the 5 mL g-C_3N_4QDs/Cu-MOF composite exhibiting the smallest charge transfer resistance. These results indicate favorable electron transport and reaction kinetics. The combined analysis demonstrates that the Cu-MOF framework enhances charge separation efficiency, while the incorporated g-C_3N_4QDs facilitate charge transfer and suppress the recombination of photogenerated electron–hole pairs, thereby improving the photocatalytic degradation activity [27].

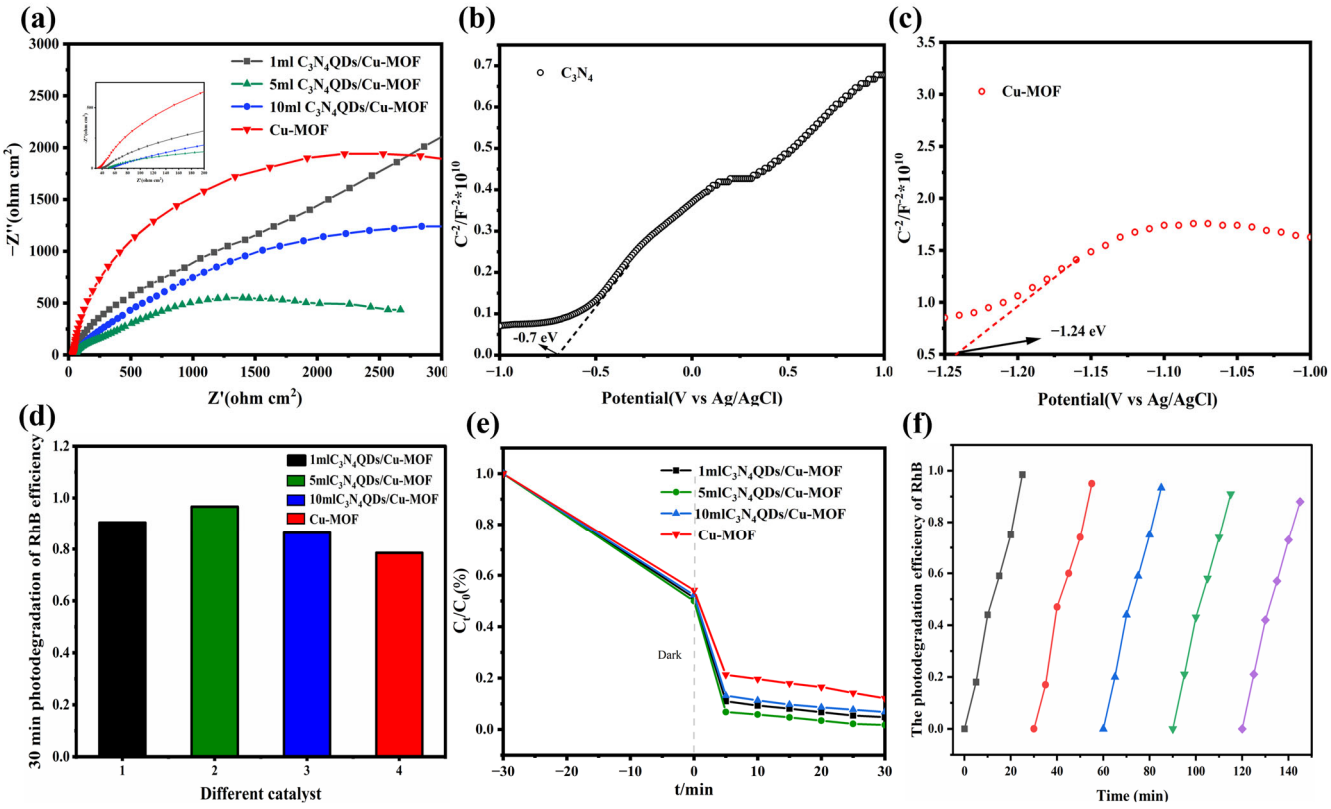


Figure 7. (**a**) EIS of the sample catalyst, (**b**) Mott-Schottky curve of C_3N_4, (**c**) The Mott-Schottky curve of Cu-MOF, (**d**) photodegradation efficiency column of sample catalyst, (**e**) photodegradation of Congo red performance in each time period of sample catalyst, (**f**) Cyclic stability test of the optimal sample catalyst.

The Mott-Schottky (M-S) plots of g-C_3N_4QDs and Cu-MOF were used to determine their respective conduction and valence band positions. When two semiconductors with appropriate band alignment come into contact, a heterojunction can form, following the relationship $E_{CB} + E_g = E_{VB}$ [47]. The M-S curves (Figure 7b,c) yield flat-band potentials corresponding to conduction band (E_{CB}) values of −0.7 eV for g-C_3N_4QDs and −1.24 eV for Cu-MOF. Combined with the optical bandgaps derived from Tauc plots (2.7 eV for g-C_3N_4 and 2.71 eV for Cu-MOF), the valence band (E_{VB}) positions are calculated as 2.0 eV for g-C_3N_4 and 1.47 eV for Cu-MOF. This band alignment conforms to a type-II heterojunction, in which photogenerated electrons transfer from the higher-lying conduction band of Cu-MOF to that of g-C_3N_4, while holes migrate in the opposite direction across the valence bands, thereby achieving efficient spatial separation of charge carriers [48].

2.3. Analysis of Photodegradation Performance

The photocatalytic performance of Cu-MOF composites with varying g-C_3N_4QD loadings was evaluated through the degradation of Congo red solution (100 mg/L). A stock solution was prepared by dissolving 25 mg of Congo red in a 250 mL volumetric flask, which was wrapped in aluminum foil and stored in the dark to prevent premature degradation. For each test, 20 mg of catalyst (Cu-MOF, 1 mL, 5 mL, or 10 mL g-C_3N_4QDs/Cu-MOF) was mixed with 100 mL of the dye solution under magnetic stirring. After a 30 min dark adsorption period, an initial sample was collected via syringe and filtered. The suspension was then irradiated under a xenon lamp simulating solar light, with filtered samples taken at 5 min intervals until no further color change was observed. As summarized in Figure 7d, the 5 mL g-C_3N_4QDs/Cu-MOF composite achieved the highest degradation efficiency of 98.3%, significantly outperforming pristine Cu-MOF (87.9%). The time-dependent degradation profiles in Figure 7e further confirm that the incorporation of g-C_3N_4QDs enhances the degradation rate, with the 5 mL loading exhibiting the most rapid and complete dye removal.

2.4. Photocatalytic Degradation Mechanism

Based on band structure analysis and photoelectrochemical characterization, the photocatalytic mechanism of the g-C_3N_4QDs/Cu-MOF composite is attributed to a synergistic oxidation process driven by a Type-II heterojunction. Under visible-light irradiation, both Cu-MOF (E_g = 2.71 eV, E_{CB} = −1.24 eV) and g-C_3N_4QDs (E_g = 2.7 eV, E_{CB} = −0.7 eV) generate electron–hole pairs. The higher conduction band potential of g-C_3N_4QDs induces electron transfer from the Cu-MOF conduction band to that of g-C_3N_4QDs, while holes migrate from the g-C_3N_4QDs valence band (E_{VB} = 2.0 eV) to the Cu-MOF valence band (E_{VB} = 1.47 eV). This directional charge separation effectively suppresses electron–hole recombination, as confirmed by the significantly reduced PL intensity [49,50], and facilitates the reduction in molecular oxygen on g-C_3N_4QDs to generate superoxide radicals ($\cdot O_2^-$) and H_2O_2, while holes accumulated in the Cu-MOF valence band directly oxidize organic pollutants or react with water to produce hydroxyl radicals (·OH). Additionally, the quantum size effect (2–5 nm) and the optimized specific surface area (273.335 m^2/g) of g-C_3N_4QDs considerably increase accessible active sites and promote mass transport and interfacial reaction kinetics [51]. The heterojunction system achieves a 98.3% degradation efficiency without external H_2O_2 addition, underscoring the essential role of rational heterostructure design in advancing the photocatalytic performance of MOF-based materials. The proposed charge transfer pathway and reactive species generation process within the g-C_3N_4QDs/Cu-MOF heterojunction are schematically illustrated in Figure 8.

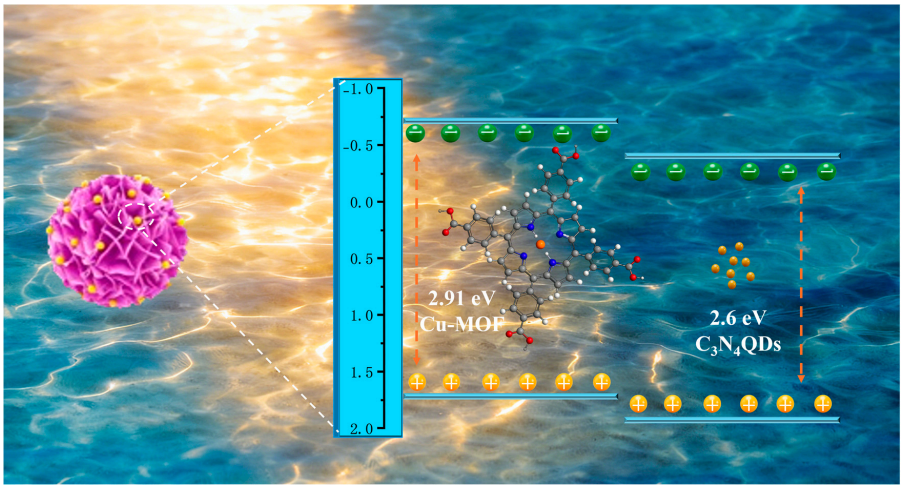


Figure 8. Mechanism diagram.

To benchmark the performance of the as-synthesized g-C_3N_4QDs/Cu-MOF composite, a comparative summary of its Congo red degradation efficiency with other representative MOF or g-C_3N_4 based photocatalysts is presented in Table 3.

Table 3. The comparison of the photocatalytic degradation efficiency obtained in this study with those reported for other catalysts based on MOF or g-C_3N_4-QDs.

Photocatalyst	Light Source	Pollutant	Degradation Efficiency	Ref.
CQDs/NH_2-MIL-125	300 W Xenon lamp	RhB	95%	[52]
g-C_3N_4/Cu-MOF	300 W Xenon lamp	Microcystic toxins	90%	[37]
CQDs/MIL-53(Fe)	500 W Xenon lamp	RhB + Cr(VI)	98%	[42]
g-C_3N_4/TiO_2	350 W Xenon lamp	Methyl orange	90%	[53]
g-C_3N_4 QDs/Cu-MOF	300 W Xenon lamp	Congo Red	96.6%	This work

3. Experimental Section

3.1. Materials and Chemicals

4-Formylbenzoic acid ($C_8H_8O_3$) was supplied by Shanghai Yuanye Bio-Technology Co., Ltd. (Shanghai, China). N,N-Dimethylformamide was obtained from Tianjin Fuyu Fine Chemical Co., Ltd. (Tianjin, China). Pyrrole (C_4H_5N) was provided by Shanghai Yayu Pharmaceutical Co., Ltd. (Shanghai, China). Propanoic acid (CH_3CH_2COOH) was sourced from Shandong Weijin Chemical Co., Ltd. (Zibo, China). Trisodium citrate was purchased from Shanghai Macklin Biochemical Co., Ltd. (Shanghai, China). A 5% Nafion solution was acquired from Shanghai Chuxi Industrial Co., Ltd. (Shanghai, China). and deionized water was used throughout all experiments.

Crystal structures were characterized by X-ray diffraction (XRD) using a Rigaku MiniFlex600 diffractometer. (Tokyo, Japan). Morphological analysis was conducted with a JEOL JSM-7900F scanning electron microscope (SEM) (Tokyo, Japan) and a JEOL JEM-2100PLUS transmission electron microscope (TEM). (Tokyo, Japan). Specific surface area and pore size distribution were determined by nitrogen physisorption measurements on a Beijing Builder SSA-4300 analyzer. (Beijing, China). Electrochemical properties were evaluated using a CHI760E electrochemical workstation (Shanghai Chenhua). (Shanghai, China). UV-visible diffuse reflectance spectra (UV-Vis DRS) were recorded on a Shimadzu UV-2700i spectrophotometer (Tokyo, Japan), while fluorescence signals were measured with a Hamamatsu H1461P-11 photomultiplier tube (Hamamatsu, Japan) coupled to a time-resolved single-photon counting system.

3.2. Preparation of Tcpp

6.08 g of 4-formylbenzoic acid and 2.8 mL of pyrrole were weighed using an analytical balance, mixed with 150 mL of propanoic acid measured by a pipette in a 200 mL beaker, and ultrasonicated for 3–5 min. The mixture was subjected to oil-bath heating under reflux for 2 h. After cooling to room temperature, 200 mL of methanol was added, followed by ice-bath stirring for 30 min. The product was isolated by centrifugation and washed repeatedly with methanol and distilled water until the filtrate became clear. The resulting solid was dried in an oven at 60 °C for 12–16 h to obtain a purple powder.

3.3. Preparation of Cu-Tcpp

0.261 g of TCPP and 0.245 g of $CuCl_2$ were weighed and dissolved in 15 mL of N,N-dimethylformamide. The mixture was subjected to oil-bath heating under reflux for 5 h, yielding a red solution. After cooling to room temperature, the solution was centrifuged and the precipitate was washed repeatedly with deionized water over seven times. The solid product was then dried in a vacuum oven at 60 °C to obtain a red powder.

3.4. Synthetic Copper-Based Mof

34 mg of Cu-TCPP and 27 mg of $CuCl_2$ were added to 12 mL of a mixed solvent consisting of N,N-dimethylformamide and ethanol in a volume ratio of 3:1. The mixture was ultrasonicated for 3–5 min and then subjected to a solvothermal reaction at 110 °C for 72 h. After cooling to room temperature, the resulting product was collected by centrifugation and washed thoroughly with ethanol and distilled water for more than five cycles. The precipitate was dried in a vacuum oven at 60 °C to obtain the Cu-MOF material.

3.5. Synthesis of C_3N_4QDs

A mixture of 1.01 g urea and 0.81 g trisodium citrate was thoroughly ground and placed in a crucible, followed by heating at 180 °C for 1.5 h to obtain quantum dot (QD) powder. The product was washed with methanol 5–6 times to remove impurities and dried in an oven. Subsequently, 100 mg of the resulting g-C_3N_4QD powder was dissolved in 10 mL of deionized water and dialyzed using a 10 kDa molecular weight cut-off membrane. The purified solution was stored for subsequent use as a photocatalyst in the synthesis of metal nanoparticles.

3.6. Preparation of Cu-Mof/C_3N_4QDs

Three 20 mg portions of Cu-MOF were separately weighed and placed into 50 mL centrifuge tubes, each containing 10 mL of ethanol. To these suspensions, 1 mL, 5 mL, and 10 mL of g-C_3N_4QDs dispersion were added. After thorough mixing and ultrasonication for 3–5 min, the mixtures were stirred for 4 h. The resulting products were collected by centrifugation and dried in a vacuum oven to obtain red powders.

3.7. The Electrochemical and Photoelectrochemical Measurements

FTO glass substrates with an area of approximately 2 cm^2 were sequentially cleaned with deionized water and ethanol in an ultrasonic bath, followed by drying in an oven. A homogeneous ink was prepared by dispersing 2 mg of the sample in a mixture of 0.45 mL ethanol and 50 μL Nafion solution, which was then drop-cast onto the substrate to form a uniform film with a controlled area of 1 cm^2. The coated electrodes were dried prior to electrochemical measurements. All electrochemical analyses, including photocurrent response and electrochemical impedance spectroscopy (EIS), were performed on a CHI760E electrochemical workstation using a standard three-electrode configuration with a saturated Ag/AgCl reference electrode, a platinum counter electrode, and the prepared sample as the working electrode in 0.5 mol/L Na_2SO_4 aqueous electrolyte. A xenon lamp system was employed as the light source during photocurrent measurements. (This experiment was independently repeated at least three times to confirm the reproducibility of the results.)

3.8. Light Degradation Performance Test

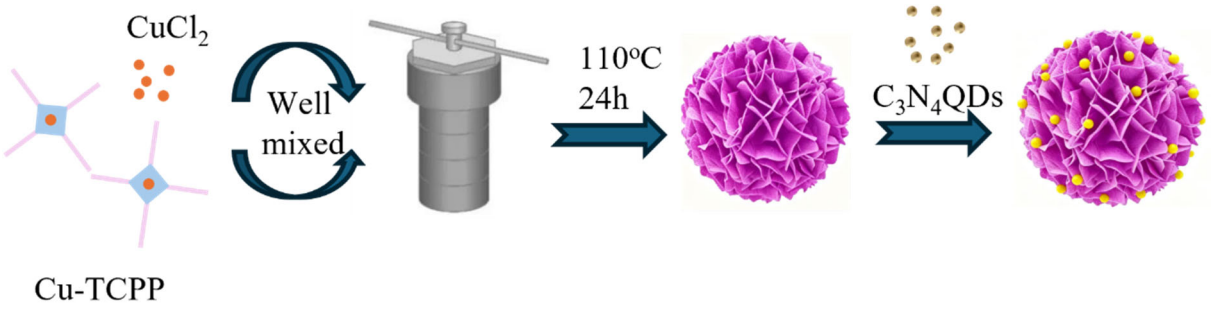
The photocatalytic degradation efficiency of the synthesized catalysts was evaluated using Rhodamine B (RhB) and Congo red as model pollutants. For each test, 20 mg of photocatalyst was introduced into a quartz reactor containing 100 mL of Congo red solution (100 mg/L). The suspension was first stirred in darkness for 30 min to establish adsorption–desorption equilibrium. A 300 W xenon lamp equipped with an AM 1.5G filter was then activated to initiate the photocatalytic reaction. During irradiation, samples were collected at 5 min intervals and filtered for analysis until the solution became colorless or exhibited no further change in absorbance. The concentration of Congo red was monitored by measuring the absorbance at its characteristic wavelength using UV-Vis spectroscopy. After each degradation experiment, the photocatalyst was recovered by centrifugation,

washed thoroughly with deionized water, and dried overnight at 60 °C for reuse. The degradation efficiency (η) was calculated according to Equation (1):

$$\eta = \frac{A_0 - A_t}{A_0} * 100\% \quad (1)$$

where A_0 and A_t represent the absorbance of the Congo red solution at the beginning of illumination and at time t, respectively (This experiment was independently repeated at least three times to confirm the reproducibility of the results). The suspension was first stirred in darkness for 30 min to establish the adsorption–desorption equilibrium. The concentration at the end of this period was defined as the initial concentration (C_0) for calculating the photocatalytic degradation efficiency, thereby isolating the contribution of pure photocatalytic action from that of adsorption.

The overall preparation process of the g-C_3N_4 QDs/Cu-MOF composite photocatalyst is visually summarized in Scheme 1. Briefly, the TCPP organic ligand was first synthesized via a condensation reaction between pyrrole and 4-formylbenzoic acid in propanoic acid. The resulting TCPP was then metallated with Cu^{2+} ions to form the Cu-TCPP complex, which served as the primary building unit for the subsequent solvothermal crystallization of the three-dimensional Cu-MOF structure. In a parallel pathway, g-C_3N_4 QDs were fabricated through a one-step thermal treatment of a urea and trisodium citrate mixture. Finally, the composite was obtained by uniformly depositing the as-synthesized g-C_3N_4 QDs onto the pre-formed Cu-MOF substrate through a facile solution-based self-assembly strategy, leveraging the interactions between the two components.



Scheme 1. Schematic illustration of the stepwise synthesis of the g-C_3N_4 QDs/Cu-MOF composite, including the preparation of Cu-MOF, synthesis of g-C_3N_4 QDs, and their final composite formation.

4. Conclusions

In this work, a heterojunction composite photocatalyst was successfully constructed by immobilizing g-C_3N_4 quantum dots (QDs) onto a Cu-MOF substrate. The loading amount of g-C_3N_4 QDs was systematically optimized (1, 5, and 10 mL), with the 5 mL composite exhibiting the best performance. This optimal composite demonstrated a significantly enhanced specific surface area of 273.335 m^2/g, representing a 143% increase compared to the pristine Cu-MOF (112.257 m^2/g). Moreover, its visible-light absorption range was notably broadened, accompanied by a reduced optical bandgap of 2.68 eV.

Electrochemical and photoluminescence analyses confirmed that the composite facilitates efficient charge separation and transfer. It achieved a photocurrent density of 1.1 $\mu A \cdot cm^{-2}$, which is 1.38 times higher than that of pure Cu-MOF, along with a lower interfacial charge transfer resistance and suppressed photoluminescence intensity.

In photocatalytic degradation tests under visible light, the 5 mL g-C_3N_4 QDs/Cu-MOF composite degraded 98.3% of Congo red (100 mg/L) within 30 min, substantially outperforming the pristine Cu-MOF (87.9%). These enhancements are attributed to the synergistic effects of the heterojunction structure, which improves light harvesting, promotes the

separation and transfer of photogenerated charge carriers, and provides a larger active surface area. With excellent stability and recyclability, this g-C_3N_4 QDs/Cu-MOF composite presents a promising and practical candidate for the design of efficient MOF-based photocatalysts and the treatment of dye-contaminated wastewater.

Author Contributions: Conceptualization, Q.L. and Y.W.; methodology, Y.Y.; software, K.W.; validation, X.Z., Y.Y. and K.W.; formal analysis, Y.W. and K.W.; investigation, X.Z. and Y.S.; resources, Q.L.; data curation, K.W.; writing—original draft preparation, Y.W.; writing—review and editing, Y.W. and Q.L.; visualization, K.W.; supervision, K.W.; project administration, Q.L.; funding acquisition, Q.L. All authors have read and agreed to the published version of the manuscript.

Funding: This work was supported by Henan Provincial Science and Technology Research Project (252102320358, 252102311248), Interdisciplinary Sciences Project of Nanyang Institute of Technology (24NGJY004), Key Scientific Research Project Plans of Higher Education Institutions in Henan Province (25A610013).

Data Availability Statement: Data will be made available on request.

Conflicts of Interest: The authors declare that they have no known competing financial interests or personal relationships that could have appeared to influence the work reported in this paper.

References

1. Skorjanc, T.; Shetty, D.; Trabolsi, A. Pollutant removal with organic macrocycle-based covalent organic polymers and frameworks. *Chem* **2021**, *7*, 882–918. [CrossRef]
2. Rojas, S.; Horcajada, P. Metal-Organic Frameworks for the Removal of Emerging Organic Contaminants in Water. *Chem. Rev.* **2020**, *16*, 8378–8415. [CrossRef]
3. Gong, P.; Xu, H.; Wang, C.; Chen, Y.; Guo, L.; Wang, X. Persistent organic pollutant cycling in forests. *Nat. Rev. Earth Environ.* **2021**, *2*, 182–197. [CrossRef]
4. Wang, X.; Ren, L.; Long, T.; Geng, C.; Tian, X. Migration and remediation of organic liquid pollutants in porous soils and sedimentary rocks: A review. *Environ. Chem. Lett.* **2022**, *21*, 479–496. [CrossRef]
5. Chen, Z.; Lu, Y.-L.; Wang, L.; Xu, J.; Zhang, J.; Xu, X.; Cheng, P.; Yang, S.; Shi, W. Efficient Recognition and Removal of Persistent Organic Pollutants by a Bifunctional Molecular Material. *J. Am. Chem. Soc.* **2022**, *145*, 260–267. [CrossRef] [PubMed]
6. Morin-Crini, N.; Lichtfouse, E.; Fourmentin, M.; Ribeiro, A.R.L.; Noutsopoulos, C.; Mapelli, F.; Fenyvesi, É.; Vieira, M.G.A.; Picos-Corrales, L.A.; Moreno-Piraján, J.C.; et al. Removal of emerging contaminants from wastewater using advanced treatments. A review. *Environ. Chem. Lett.* **2022**, *20*, 1333–1375. [CrossRef]
7. Jain, B.; Singh, A.K.; Kim, H.; Lichtfouse, E.; Sharma, V.K. Treatment of organic pollutants by homogeneous and heterogeneous Fenton reaction processes. *Environ. Chem. Lett.* **2018**, *16*, 947–967. [CrossRef]
8. Grandclément, C.; Seyssiecq, I.; Piram, A.; Wong-Wah-Chung, P.; Vanot, G.; Tiliacos, N.; Roche, N.; Doumenq, P. From the conventional biological wastewater treatment to hybrid processes, the evaluation of organic micropollutant removal: A review. *Water Res.* **2017**, *111*, 297–317. [CrossRef]
9. Zhang, X.; Wang, J.; Dong, X.-X.; Lv, Y.-K. Functionalized metal-organic frameworks for photocatalytic degradation of organic pollutants in environment. *Chemosphere* **2019**, *242*, 125144. [CrossRef]
10. Silvestri, S.; Fajardo, A.R.; Iglesias, B.A. Supported porphyrins for the photocatalytic degradation of organic contaminants in water: A review. *Environ. Chem. Lett.* **2021**, *20*, 731–771. [CrossRef]
11. Gusain, R.; Gupta, K.; Joshi, P.; Khatri, O.P. Adsorptive removal and photocatalytic degradation of organic pollutants using metal oxides and their composites: A comprehensive review. *Adv. Colloid Interface Sci.* **2019**, *272*, 102009. [CrossRef]
12. Kiwaan, H.A.; Atwee, T.M.; Azab, E.A.; El-Bindary, A.A. Efficient photocatalytic degradation of Acid Red 57 using synthesized ZnO nanowires. *J. Chin. Chem. Soc.* **2018**, *66*, 89–98. [CrossRef]
13. El-Dossoki, F.I.; Atwee, T.M.; Hamada, A.M.; El-Bindary, A.A. Photocatalytic degradation of Remazol Red B and Rhodamine B dyes using TiO_2 nanomaterial: Estimation of the effective operating parameters. *Desalination Water Treat.* **2021**, *233*, 319–330. [CrossRef]
14. Kiwaan, H.A.; Atwee, T.M.; Azab, E.A.; El-Bindary, A.A. Photocatalytic degradation of organic dyes in the presence of nanostructured titanium dioxide. *J. Mol. Struct.* **2020**, *1200*, 127115. [CrossRef]
15. Zheng, Z.; Tian, S.; Feng, Y.; Zhao, S.; Li, X.; Wang, S.; He, Z. Recent advances of photocatalytic coupling technologies for wastewater treatment. *Chin. J. Catal.* **2023**, *54*, 88–136. [CrossRef]

16. Ju, Y.; Wang, Z.; Lin, H.; Hou, R.; Li, H.; Wang, Z.; Zhi, R.; Lu, X.; Tang, Y.; Chen, F. Modulating the microenvironment of catalytic interface with functional groups for efficient photocatalytic degradation of persistent organic pollutants. *Chem. Eng. J.* **2023**, *479*, 147800. [CrossRef]
17. Chen, C.; Fei, L.; Wang, B.; Xu, J.; Li, B.; Shen, L.; Lin, H. MOF-Based Photocatalytic Membrane for Water Purification: A Review. *Small* **2023**, *20*, 2305066. [CrossRef] [PubMed]
18. Cao, C.-S.; Wang, J.; Yu, X.; Zhang, Y.; Zhu, L. Photodegradation of seven bisphenol analogues by Bi5O7I/UiO-67 heterojunction: Relationship between the chemical structures and removal efficiency. *Appl. Catal. B Environ. Energy* **2020**, *277*, 119222. [CrossRef]
19. Furukawa, H.; Cordova, K.E.; O'Keeffe, M.; Yaghi, O.M. The chemistry and applications of metal-organic frameworks. *Science* **2013**, *341*, 1230444. [CrossRef]
20. Gao, Y.; Xia, J.; Liu, D.; Kang, R.; Yu, G.; Deng, S. Synthesis of mixed-linker Zr-MOFs for emerging contaminant adsorption and photodegradation under visible light. *Chem. Eng. J.* **2019**, *378*, 122118. [CrossRef]
21. Hiroto, S.; Miyake, Y.; Shinokubo, H. Synthesis and Functionalization of Porphyrins through Organometallic Methodologies. *Chem. Rev.* **2016**, *117*, 2910–3043. [CrossRef]
22. Lu, L.; Li, L.; Chu, M.; Chen, C.; Wang, B.; Wang, J.; Shen, Y.; Ma, R.; Li, B.; Shen, L.; et al. Recent Advancement in 2D Metal–Organic Framework for Environmental Remediation: A Review. *Adv. Funct. Mater.* **2024**, *35*, 2419433. [CrossRef]
23. Zhu, X.; Zhou, E.; Tai, X.; Zong, H.; Yi, J.; Yuan, Z.; Zhao, X.; Huang, P.; Xu, H.; Jiang, Z. g-C(3)N(4) S-Scheme Homojunction through Van der Waals Interface Regulation by Intrinsic Polymerization Tailoring for Enhanced Photocatalytic H(2) Evolution and CO(2) Reduction. *Angew. Chem. Int. Ed. Engl.* **2025**, *64*, e202425439. [CrossRef] [PubMed]
24. Shang, S.; Xiong, W.; Yang, C.; Johannessen, B.; Liu, R.; Hsu, H.-Y.; Gu, Q.; Leung, M.K.H.; Shang, J. Atomically Dispersed Iron Metal Site in a Porphyrin-Based Metal–Organic Framework for Photocatalytic Nitrogen Fixation. *ACS Nano* **2021**, *15*, 9670–9678. [CrossRef]
25. Wang, Z.; Li, Q.; Su, R.; Lv, G.; Wang, Z.; Gao, B.; Zhou, W. Enhanced degradation of bisphenol F in a porphyrin-MOF based visible-light system under high salinity conditions. *Chem. Eng. J.* **2022**, *428*, 132106. [CrossRef]
26. Lv, S.-W.; Cong, Y.; Chen, X.; Wang, W.; Che, L. Developing fine-tuned metal-organic frameworks for photocatalytic treatment of wastewater: A review. *Chem. Eng. J.* **2021**, *433*, 133605. [CrossRef]
27. Chen, J.; Qin, C.; Mou, Y.; Cao, Y.; Chen, H.; Yuan, X.; Wang, H. Linker regulation of iron-based MOFs for highly effective Fenton-like degradation of refractory organic contaminants. *Chem. Eng. J.* **2023**, *459*, 141588. [CrossRef]
28. Wang, S.; Hu, G.; Dou, Y.; Li, S.; Li, M.; Feng, H.; Feng, Y.-S. Z-scheme promoted interfacial charge transfer on Cu/In-porphyrin MOFs/$CdIn_2S_4$ heterostructure for efficient photocatalytic H_2 evolution. *Sep. Purif. Technol.* **2024**, *354*, 129220. [CrossRef]
29. Anagnostopoulou, M.; Keller, V.; Christoforidis, K.C. Cu-Metalated Porphyrin-Based MOFs Coupled with Anatase as Photocatalysts for CO_2 Reduction: The Effect of Metalation Proportion. *Energies* **2024**, *17*, 1483. [CrossRef]
30. Shi, Y.; Yang, Y.; Ge, S.; Wu, M.; Jiang, J.; Fan, W.; Debecker, D.P.; Rezakazemi, M.; Zhang, Z. Progress in advanced MOF-derived materials for the removal of organic and inorganic pollutants. *Coord. Chem. Rev.* **2025**, *530*, 216474. [CrossRef]
31. Tan, Y.; Chen, X.; Yuan, J.; Sheng, G.; Deng, W.Q.; Wu, H. Concentration-Adaptive Electrocatalytic Urea Synthesis from CO_2 and Nitrate via Porphyrin and Metalloporphyrin MOFs. *Angew. Chem. Int. Ed.* **2025**, *64*, e202513441. [CrossRef]
32. Majdoub, M.; Sengottuvelu, D.; Nouranian, S.; Al-Ostaz, A. Graphitic Carbon Nitride Quantum Dots (g-C_3N_4 QDs): From Chemistry to Applications. *ChemSusChem* **2024**, *17*, e202301462. [CrossRef]
33. Wang, J.; Wang, S. A critical review on graphitic carbon nitride (g-C_3N_4)-based materials: Preparation, modification and environmental application. *Coord. Chem. Rev.* **2022**, *453*, 214338. [CrossRef]
34. Nxele, S.R.; Nyokong, T. Time-dependent characterization of graphene quantum dots and graphitic carbon nitride quantum dots synthesized by hydrothermal methods. *Diam. Relat. Mater.* **2022**, *121*, 108751. [CrossRef]
35. Chen, H.-R.; Meng, W.-M.; Wang, R.-Y.; Chen, F.-L.; Li, T.; Wang, D.-D.; Wang, F.; Zhu, S.-E.; Wei, C.-X.; Lu, H.-D.; et al. Engineering highly graphitic carbon quantum dots by catalytic dehydrogenation and carbonization of $Ti_3C_2T_x$-MXene wrapped polystyrene spheres. *Carbon* **2022**, *190*, 319–328. [CrossRef]
36. Shi, Q.; Li, Z.; Chen, L.; Zhang, X.; Han, W.; Xie, M.; Yang, J.; Jing, L. Synthesis of SPR Au/$BiVO_4$ quantum dot/rutile-TiO_2 nanorod array composites as efficient visible-light photocatalysts to convert CO_2 and mechanism insight. *Appl. Catal. B Environ.* **2019**, *244*, 641–649. [CrossRef]
37. Wang, Z.; Xu, Y.; Wang, C.; Yue, L.; Liu, T.; Lan, Q.; Cao, X.; Xing, B. Photocatalytic inactivation of harmful algae Microcystis aeruginosa and degradation of microcystin by g-C_3N_4/Cu-MOF nanocomposite under visible light. *Sep. Purif. Technol.* **2023**, *313*, 123515. [CrossRef]
38. Wang, Q.; Wang, G.; Liang, X.; Dong, X.; Zhang, X. Supporting carbon quantum dots on NH_2-MIL-125 for enhanced photocatalytic degradation of organic pollutants under a broad spectrum irradiation. *Appl. Surf. Sci.* **2019**, *467–468*, 320–327. [CrossRef]
39. Xie, S.; Deng, C.; Huang, Q.; Zhang, C.; Chen, C.; Zhao, J.; Sheng, H. Facilitated Photocatalytic CO_2 Reduction in Aerobic Envi-ronment on a Copper-Porphyrin Metal–Organic Framework. *Angew. Chem. Int. Ed.* **2023**, *62*, e202216717. [CrossRef]

40. Zhao, C.; Yang, X.; Zhao, B.; Zhang, Z.; Guo, W.; Shen, A.; Ye, M.; Wang, W. Copper porphyrin MOF/graphene oxide composite membrane with high efficiency electrocatalysis and structural stability for wastewater treatment. *J. Membr. Science* **2024**, *695*, 122. [CrossRef]
41. Wu, K.; Peng, B.; Yu, Q.; Liu, Q.; Li, B.; Tian, J.; Liu, Z.; Tai, Y. Bifunctional coupled metal covalent organic framework MCOF-FeCu is used to implement bionic leaves. *Fuel* **2025**, *400*, 135787. [CrossRef]
42. He, Z.; Liang, R.; Zhou, C.; Yan, G.; Wu, L. Carbon quantum dots (CQDs)/noble metal co-decorated MIL-53(Fe) as difunctional photocatalysts for the simultaneous removal of Cr(VI) and dyes. *Sep. Purif. Technol.* **2021**, *255*, 117725. [CrossRef]
43. Chen, J.; Lv, S.; Shen, Z.; Tian, P.; Chen, J.; Li, Y. Novel ZnCdS Quantum Dots Engineering for Enhanced Visible-Light-Driven Hydrogen Evolution. *ACS Sustain. Chem. Eng.* **2019**, *7*, 13805–13814. [CrossRef]
44. Fan, W.; Chang, H.; Zhong, J.; Lu, J.; Ma, G.; Zhang, H.; Jiang, Z.; Yin, G. Facile synthesis of ZnCdS quantum dots via a novel photoetching MOF strategy for boosting photocatalytic hydrogen evolution. *Sep. Purif. Technol.* **2023**, *330*, 125258. [CrossRef]
45. Jia, J.; Liang, Y.; Yang, G.; Yang, J.; Zhang, X.; Zeng, Z.; Yang, Z.; Xu, S.; Han, C. Reinforced $AgFeO_2$-Bi_4TaO_8Cl p-n heterojunction with facet-assisted photocarrier separation for boosting photocatalytic degradation of ofloxacin. *Sep. Purif. Technol.* **2023**, *322*, 124333. [CrossRef]
46. Wu, X.; Cheng, J.; Li, X.; Li, Y.; Lv, K. Enhanced Visible Photocatalytic Oxidation of NO by Repeated Calcination of g-C_3N_4. *Appl. Surf. Sci.* **2019**, *465*, 1037–1046. [CrossRef]
47. Molaei, M.J. Graphitic carbon nitride (g-C_3N_4) synthesis and heterostructures, principles, mechanisms, and recent advances: A critical review. *Int. J. Hydrogen Energy* **2023**, *48*, 32708–32728. [CrossRef]
48. Rajaitha, P.M.; Shamsa, K.; Murugan, C.; Bhojanaa, K.B.; Ravichandran, S.; Jothivenkatachalam, K.; Pandikumar, A. Graphitic carbon nitride nanoplatelets incorporated titania based type-II heterostructure and its enhanced performance in photoelectrocatalytic water splitting. *SN Appl. Sci.* **2020**, *2*, 572. [CrossRef]
49. Akanksha; Kundu, S.; Dhariwal, N.; Yadav, P.; Kumar, V.; Singh, A.K.; Thakur, S. Coordinated environmental and hydrogen energy resilience: A chronological insight into dual functional photocatalysts. *Coord. Chem. Rev.* **2025**, *541*, 216782. [CrossRef]
50. Wu, M.; Lv, C.; Xiong, Y.; Li, W.; Lin, Y.; Li, J.; Yu, F.; Yuan, H.; You, B.; Zhang, Q.; et al. Heterojunction configuration-specific photocatalytic degradation of methyl orange and methylene blue dyes using ZnO-based nanocomposites. *J. Adv. Res.* 2025; *Online ahead of print*.
51. Du, T.; Zheng, S.; Zhang, Y.; Zhang, Y.; Wang, B.; Song, W.; Meng, C.; Zhao, Y.; Miao, Z. Recent progress in zeolite-based photocatalysts: Strategies for improving photocatalytic performance. *J. Alloys Compd.* **2025**, *1035*, 181573. [CrossRef]
52. Guselnikova, O.; Postnikov, P.; Pershina, A.; Svorcik, V.; Lyutakov, O. Express and portable label-free DNA detection and recognition with SERS platform based on functional Au grating. *Appl. Surf. Sci.* **2019**, *470*, 219–227. [CrossRef]
53. Guo, H.-A.; Jou, S.; Mao, T.-Z.; Huang, B.-R.; Huang, Y.-T.; Yu, H.-C.; Hsieh, Y.-F.; Chen, C.-C. Silicon- and oxygen-codoped graphene from polycarbosilane and its application in graphene/n-type silicon photodetectors. *Appl. Surf. Sci.* **2019**, *464*, 125–130. [CrossRef]

Disclaimer/Publisher's Note: The statements, opinions and data contained in all publications are solely those of the individual author(s) and contributor(s) and not of MDPI and/or the editor(s). MDPI and/or the editor(s) disclaim responsibility for any injury to people or property resulting from any ideas, methods, instructions or products referred to in the content.